

Active particle motion in Poiseuille flow through rectangular channels

Rahil N. Valani^{1,*}, Brendan Harding², and Yvonne M. Stokes¹

¹*School of Computer and Mathematical Sciences,*

University of Adelaide, South Australia 5005, Australia and

²*School of Mathematics and Statistics, Victoria University of Wellington, Wellington 6012, New Zealand*

(Dated: April 12, 2024)

We investigate the dynamics of a point-like active particle suspended in fluid flow through a straight channel. For this particle-fluid system, we derive a constant of motion for a general unidirectional fluid flow, and apply it to an approximation of Poiseuille flow through rectangular cross-sections. For a given rectangular cross-section, this results in a 4D nonlinear conservative dynamical system with one constant of motion and a dimensionless parameter as the ratio of maximum flow speed to intrinsic active particle speed. We observe a diverse set of active particle trajectories with variations in system parameters and initial conditions which we classify into different types of swinging, trapping, tumbling and wandering motion. Regular (periodic/quasiperiodic) motion as well as chaotic active particle motion are observed for these trajectories and quantified using largest Lyapunov exponents. We explore the transition to chaotic motion using Poincaré maps and show “sticky” chaotic tumbling trajectories that have long transients near a periodic state. Outcomes of this work may have implications for dynamics of natural and artificial microswimmers in experimental microfluidic channels that typically have rectangular cross-sections.

I. INTRODUCTION

Active particles are entities that take energy from the environment and convert it into persistent motion. Examples include macroscopic living organisms, such as birds, fish and mammals, who consume energy from food and self-propel via various modes of locomotion. Active particles are also ubiquitous in the microscopic living world such as bacteria, cells, algae and other microorganisms [1]. Although persistent motion is a visible feature that is commonly associated with life, active particles also emerge in several non-equilibrium inanimate physical and chemical systems [2–6].

Active particles immersed in a fluid medium at the micro scale, also known as microswimmers, are a commonly studied class of active particles [7]. These microswimmers ubiquitously interact with external fluid flows in various situations. For example, microswimmers routinely experience unidirectional flows in confined channels such as sperm cells swimming in fallopian tubes [8, 9], pathogens moving through blood vessels [10] and micro-robots programmed for targeted drug delivery applications [11]. In these scenarios, the coupling between external flow fields and intrinsic velocity of the active particle can lead to rich dynamical behaviors [12]. Understanding of the active particle dynamics arising from coupling with external fluid flows is not only crucial from a biological perspective, but it will also guide in design of artificial microswimmers for biomedical applications of cell manipulation, targeted drug delivery and cargo transport [13]. Further, it can guide designs of industrial and biomedical microfluidic devices aimed at focusing, sorting and filtering of microorganisms in a fluid suspension [14, 15].

Zöttl and Stark [16] studied the motion of a microswimmer in unidirectional confined flows by modeling the active particle as a spherically symmetric point with constant intrinsic velocity. For 2D planar Poiseuille flow, they showed that the equation of motion for the active particle can be mapped onto the mathematical equation of a simple pendulum, where the oscillating and circling solutions of the pendulum motion corresponds to two different types of active particle motion, swinging and tumbling, respectively. In swinging motion the upstream-oriented active particle performs oscillations about the channel centerline, whereas in tumbling motion, the active particle oscillates near the edges of the channel with fluctuating orientation and does not cross the channel centerline. Variations of this model that include additional attributes to the active particle and/or fluid flow have been investigated in detail for 2D channel flows [17–22]. For 3D cylindrical Poiseuille flow, Zöttl and Stark [16] showed that the particle-fluid dynamical system is Hamiltonian with enough conserved quantities to make the system integrable. In this case, they showed that the active particle exhibits periodic motion with 3D generalizations of swinging and tumbling trajectories. The effect of flow anisotropy was also studied by Zöttl and Stark [22] where they considered an elliptical channel cross-section and showed that the active particle motion is much more complex with typically quasiperiodic trajectories, and a few examples of chaotic motion using Poincaré maps were also reported by Zöttl [23].

Although the axisymmetric fluid flow profile in a cylindrical channel results in simplified equations for the active particle motion, in many microfluidic applications concerned with natural and artificial microswimmers, microchannels with rectangular cross-sections are more commonly used since they are relatively easy to fabricate [24]. Motivated by this, in this paper, we apply the simple model of Zöttl and Stark [16] to explore the

* rahil.valani@gmail.com

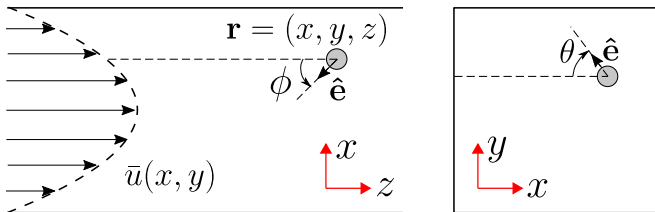


FIG. 1. Schematic of the particle-fluid system in dimensionless units. A simple point-like active particle located at $\mathbf{r} = (x, y, z)$ and having a unit intrinsic speed in the direction of its orientation $\hat{\mathbf{e}}$ is suspended in a unidirectional channel flow $\bar{u}(x, y)$ through a straight 3D rectangular channel with width to height aspect ratio AR . The particle's orientation is represented using spherical co-ordinates with polar angle $\theta \in (-\pi/2, \pi/2)$ measuring the orientation relative to the $x - z$ plane, and azimuthal angle $\phi \in (-\pi, \pi]$ measuring angle within the $x - z$ plane relative to the (negative) z axis. The left panel shows the top-view of the channel in the $x - z$ plane while the right panel shows the cross-sectional view of the channel in the $y - x$ plane.

dynamics of a simple active particle in Poiseuille flow through a straight channel having square/rectangular cross-sections. The introduction of a square/rectangular cross-section introduces anisotropy by breaking the continuous rotational symmetry of fluid flow in a circular cross-section and makes the system non-integrable. We observe a rich variety of active particle motion with both quasiperiodic and chaotic trajectories that we explore in detail as a function of system parameters and initial conditions.

The paper is organized as follows. In Sec. II we present the equations of motion for the particle-fluid system and derive general constants of motion for an active particle in unidirectional fluid flow. We then identify equilibrium states for an active particle in Poiseuille flow with rectangular cross-section and determine their stability in Sec. III. After briefly reviewing active particle motion in a channel with circular cross-section in Sec. IV, we present in Sec. V a detailed exploration of active particle dynamics in a channel with square cross-section. This includes a classification of trajectories, comparison with dynamics in a circular cross-section, a detailed parameter space exploration of cross-sectional active particle dynamics as well as an investigation of the transport of active particle along the channel. In Sec. VI we briefly explore the effect of aspect ratio of the rectangular cross-section on active particle motion. We provide our conclusions in Sec. VII.

II. EQUATIONS OF MOTION

As illustrated in Fig. 1, consider a point-like active particle model of a spherical microswimmer having a constant intrinsic swimming speed v_0 in the direction of its orientation $\hat{\mathbf{e}} = e_x \hat{\mathbf{i}} + e_y \hat{\mathbf{j}} + e_z \hat{\mathbf{k}}$. The active particle is located at $\mathbf{r} = x \hat{\mathbf{i}} + y \hat{\mathbf{j}} + z \hat{\mathbf{k}}$ and is suspended in a steady

unidirectional flow $u(x, y) \hat{\mathbf{k}}$ through a straight 3D channel. The equations of motion for the active particle are given by [16]:

$$\frac{d\mathbf{r}}{dt} = v_0 \hat{\mathbf{e}} + u(x, y) \hat{\mathbf{k}}, \quad (1)$$

$$\frac{d\hat{\mathbf{e}}}{dt} = \frac{1}{2} (\nabla \times u(x, y) \hat{\mathbf{k}}) \times \hat{\mathbf{e}}. \quad (2)$$

Equation (1) describes the translational motion of the active particle as a combination of its intrinsic velocity $v_0 \hat{\mathbf{e}}$ and the velocity of the background fluid flow at the particle location $u(x, y) \hat{\mathbf{k}}$, whereas Eq. (2) describes the evolution of the active particle's orientation based on the local flow vorticity. We assume that the active particle is small compared to the cross-sectional dimensions of the channel, and hence the particle does not disturb the fluid flow. Further, we assume that the active particle stays away from bounding walls so that we can neglect interactions/collisions between the active particle and the walls.

Non-dimensionalizing Eqs. (1) and (2) with a characteristic length scale H of the cross-section and time scale H/v_0 , we get the following dimensionless equations:

$$\frac{d\mathbf{r}}{dt} = \hat{\mathbf{e}} + \bar{u}(x, y) \hat{\mathbf{k}},$$

$$\frac{d\hat{\mathbf{e}}}{dt} = \frac{1}{2} (\nabla \times \bar{u}(x, y) \hat{\mathbf{k}}) \times \hat{\mathbf{e}}.$$

Here, $\bar{u}(x, y)$ is the dimensionless flow field (scaled by the active particle speed v_0). In Cartesian components, we get six nonlinear ordinary differential equations (ODEs) as follows:

$$\begin{aligned} \dot{x} &= e_x, \quad \dot{y} = e_y, \quad \dot{z} = e_z + \bar{u}(x, y), \\ \dot{e}_x &= -\frac{1}{2} e_z \frac{\partial \bar{u}}{\partial x}, \quad \dot{e}_y = -\frac{1}{2} e_z \frac{\partial \bar{u}}{\partial y}, \quad \dot{e}_z = \frac{1}{2} e_x \frac{\partial \bar{u}}{\partial x} + \frac{1}{2} e_y \frac{\partial \bar{u}}{\partial y}. \end{aligned} \quad (3)$$

We note from Eq. (3) that the dynamical flow is divergence free, that is $\nabla \cdot (\dot{x}, \dot{y}, \dot{z}, \dot{e}_x, \dot{e}_y, \dot{e}_z) = 0$. Hence, the dynamical system is conservative and phase-space volumes are preserved under the dynamical flow. We further note that the z variable can be decoupled i.e. the \dot{z} equation can be integrated separately, thus reducing our dynamical system to five equations. The effective dimension of our dynamical system is further reduced by identifying constants of motion, i.e. quantities that remain constant during the evolution of the system. A trivial constant of motion for our system is

$$|\hat{\mathbf{e}}|^2 = e_x^2 + e_y^2 + e_z^2 = 1, \quad (4)$$

since the orientation vector has unit magnitude. We have also identified another constant of motion as (see Appendix A for a proof)

$$H_g = -\frac{1}{2} \bar{u}(x, y) + e_z. \quad (5)$$

With these two constants of motion, our five-dimensional dynamical system reduces to three effective dimensions. We can explicitly use the constant of motion in Eq. (4) and reduce our system to four nonlinear ODEs. This is done by parameterizing the three Cartesian orientation components of the active particle, e_x, e_y and e_z using spherical co-ordinate angles θ and ϕ as follows:

$$\begin{aligned} e_x &= -\cos\theta \sin\phi, \\ e_y &= \sin\theta, \\ e_z &= -\cos\theta \cos\phi. \end{aligned}$$

Here, $\theta \in (-\pi/2, \pi/2)$ is the polar angle measuring the orientation relative to the $x-z$ plane, while $\phi \in (-\pi, \pi]$ is the azimuthal angle measuring the orientation component within the $x-z$ plane relative to the negative z axis (see Fig. 1). This parameterization gives us the following four coupled nonlinear ODEs:

$$\begin{aligned} \dot{x} &= -\cos\theta \sin\phi, \\ \dot{y} &= \sin\theta, \\ \dot{\theta} &= \frac{1}{2} \frac{\partial \bar{u}}{\partial y} \cos\phi, \\ \dot{\phi} &= \frac{1}{2} \frac{\partial \bar{u}}{\partial y} \tan\theta \sin\phi - \frac{1}{2} \frac{\partial \bar{u}}{\partial x}, \end{aligned} \quad (6)$$

along with one constant of motion in Eq. (5) which is rewritten in the above parameterization as

$$H_g = -\frac{1}{2} \bar{u}(x, y) - \cos\phi \cos\theta. \quad (7)$$

We note that up to this point, our consideration of the fluid flow field $\bar{u}(x, y)$ has been general and hence the constant of motion in Eq. (5) exists independent of the specific flow profile.

We now consider the specific fluid flow profile of Poiseuille flow in a 3D straight channel having a rectangular cross-section with width W and height H . We approximate this flow profile by

$$u(x, y) = U_0 \left(1 - \left(\frac{x}{W}\right)^2\right) \left(1 - \left(\frac{y}{H}\right)^2\right).$$

This expression provides a good approximation to the exact solution of Poiseuille flow in rectangular channels expressed as an infinite series (see Appendix B). In dimensionless form (with channel height H as the length scale and H/v_0 as the time scale), our flow field is given by

$$\bar{u}(x, y) = \bar{U} \left(1 - \left(\frac{x}{AR}\right)^2\right) (1 - y^2), \quad (8)$$

where $\bar{U} = U_0/v_0$, is the ratio of maximum flow speed to the intrinsic active particle speed and $AR = W/H$, is the aspect ratio of the rectangular cross-section. Substituting this flow field in Eq. (6) we get the following 4D

dynamical system (along with the constant of motion in Eq. (7)):

$$\begin{aligned} \dot{x} &= -\cos\theta \sin\phi, \\ \dot{y} &= \sin\theta, \\ \dot{\theta} &= -\bar{U}y \cos\phi \left(1 - \left(\frac{x}{AR}\right)^2\right), \\ \dot{\phi} &= -\bar{U}y \tan\theta \sin\phi \left(1 - \left(\frac{x}{AR}\right)^2\right) + \bar{U} \frac{x}{AR^2} (1 - y^2), \end{aligned} \quad (9)$$

where $-AR < x < AR$, $-1 < y < 1$, $-\pi/2 < \theta < \pi/2$, $-\pi < \phi \leq \pi$ and $z \in \mathbb{R}$.

We solve the dynamical system in Eq. (9) up to $t = 1000$ (unless stated otherwise) using the ode45 solver in MATLAB with relative and absolute tolerance of 10^{-10} . These very small tolerances ensure that numerical variations in the constants of motion are less than 10^{-8} for the duration of simulations.

III. EQUILIBRIUM STATES AND STABILITY

We start by finding equilibrium states of the dynamical system that would correspond to an active particle with a fixed cross-sectional location and a fixed orientation. This is done by making the time derivatives zero in Eq. (9) and solving the resulting nonlinear algebraic equations. We get the following two equilibrium states:

$$(x^*, y^*, \theta^*, \phi^*) = (0, 0, 0, 0) \ \& \ (0, 0, 0, \pi).$$

The former equilibrium state, $(x^*, y^*, \theta^*, \phi^*) = (0, 0, 0, 0)$, corresponds to an active particle oriented upstream at the center of the channel, while the latter state, $(x^*, y^*, \theta^*, \phi^*) = (0, 0, 0, \pi)$, corresponds to an active particle oriented downstream at the center of the channel.

To understand the stability of these equilibrium states, we perform a linear stability analysis by perturbing the equilibrium states as follows: $(x, y, \theta, \phi) = (x^*, y^*, \theta^*, \phi^*) + \epsilon(x_1, y_1, \theta_1, \phi_1)$, where $\epsilon > 0$ is a perturbation parameter. Substituting this in Eq. (9) and comparing $O(\epsilon)$ terms we get a matrix equation for the evolution of perturbation variables $(x_1, y_1, \theta_1, \phi_1)$.

1. Upstream-oriented equilibrium state

For the upstream-oriented equilibrium state $(x^*, y^*, \theta^*, \phi^*) = (0, 0, 0, 0)$, we obtain the following matrix equation that governs the evolution of perturbations:

$$\begin{bmatrix} \dot{x}_1 \\ \dot{y}_1 \\ \dot{\theta}_1 \\ \dot{\phi}_1 \end{bmatrix} = \begin{bmatrix} 0 & 0 & 0 & -1 \\ 0 & 0 & 1 & 0 \\ 0 & -\bar{U} & 0 & 0 \\ \bar{U}/AR^2 & 0 & 0 & 0 \end{bmatrix} \begin{bmatrix} x_1 \\ y_1 \\ \theta_1 \\ \phi_1 \end{bmatrix}.$$

The stability of the equilibrium state is determined by the nature of the eigenvalues of the right-hand-side matrix [25]. We get the following characteristic polynomial equation for eigenvalues λ :

$$\lambda^4 + \bar{U} \left(1 + \frac{1}{AR^2} \right) \lambda^2 + \frac{\bar{U}^2}{AR^2}.$$

The roots of this quartic polynomial gives the eigenvalues:

$$\lambda = \pm i\sqrt{\bar{U}}, \pm i\frac{\sqrt{\bar{U}}}{AR}.$$

Thus, all the eigenvalues are purely imaginary for this upstream-oriented active particle state. This equilibrium state may correspond to a center or a stable/unstable spiral [25], however, the conservative nature of our dynamical system makes this equilibrium point a center and we will revisit this numerically in Sec. V C. Furthermore, due to the aspect ratio of the channel differing from $AR = 1$ for non-square cross-sections, the oscillation frequency coming from the imaginary part of the eigenvalues is different in directions corresponding to the eigenvectors.

2. Downstream-oriented equilibrium state

For the downstream-oriented equilibrium state $(x^*, y^*, \theta^*, \phi^*) = (0, 0, 0, \pi)$, we get the following matrix equation for evolution of perturbations:

$$\begin{bmatrix} \dot{x}_1 \\ \dot{y}_1 \\ \dot{\theta}_1 \\ \dot{\phi}_1 \end{bmatrix} = \begin{bmatrix} 0 & 0 & 0 & 1 \\ 0 & 0 & 1 & 0 \\ 0 & \bar{U} & 0 & 0 \\ \bar{U}/AR^2 & 0 & 0 & 0 \end{bmatrix} \begin{bmatrix} x_1 \\ y_1 \\ \theta_1 \\ \phi_1 \end{bmatrix},$$

with the following characteristic equation,

$$\lambda^4 - \bar{U} \left(1 + \frac{1}{AR^2} \right) \lambda^2 + \frac{\bar{U}^2}{AR^2}.$$

Solving this quartic polynomial gives us the eigenvalues

$$\lambda = \pm\sqrt{\bar{U}}, \pm\frac{\sqrt{\bar{U}}}{AR}.$$

Since the eigenvalues are all real and both positive and negative, this equilibrium state is a saddle point having both stable and unstable manifolds. Hence this state is unstable. Again, due to the different magnitude of eigenvalues for non-square cross-sections, the rate of instability from the saddle point differs in the directions of the corresponding eigenvectors. We will numerically revisit the dynamics of an active particle starting near this equilibrium state in Sec. V C.

IV. DYNAMICS IN A CYLINDRICAL CHANNEL

Zöttl and Stark [16] studied the nonlinear dynamics of an active particle suspended in fluid flow through a

cylindrical channel. For a circular cross-section, the flow field is axisymmetric and takes the form (in dimensionless form with length variables scaled with the duct radius)

$$\bar{u}_c(x, y) = \bar{U} (1 - (x^2 + y^2)). \quad (10)$$

For this system, they identified two constants of motion as follows:

$$H_c = \frac{1}{2}\bar{U}(x^2 + y^2) + 1 - \cos\phi \cos\theta, \quad (11)$$

and

$$L_z = x \sin\theta + y \cos\theta \sin\phi. \quad (12)$$

Here H_c is a linear transform of the general constant of motion identified in Eq. (7). The new constant of motion L_z arises from the continuous rotational symmetry of the circular cross-section and it is proportional to the angular momentum of the active particle in the z direction. This additional constant of motion further reduces the effective dimension of the dynamical system in Eq. (6) from three to two dimensions. By making a change of co-ordinates, Zöttl and Stark [16] obtained three nonlinear ODEs with the two constants of motion H_c and L_z , and showed that the active particle motion in a cylindrical channel results in an integrable Hamiltonian system where the motion in the three-dimensional phase-space is restricted to a curve formed by the intersection of two surfaces corresponding to H_c and L_z .

V. DYNAMICS IN A SQUARE CHANNEL

We now explore in detail the dynamics of an active particle suspended in fluid flow through a 3D straight channel with a square cross-section i.e. $AR = 1$. We explore the active particle dynamics as a function of the dimensionless parameter \bar{U} as well as the initial conditions i.e. the initial position in the cross-section $(x(0), y(0))$, and the initial orientation angles $(\theta(0), \phi(0))$.

A. Classification of active particle trajectories

A large diversity of trajectories are observed for the active particle in a square channel by varying the system parameter \bar{U} as well as the initial conditions. Some typical trajectories and the corresponding orientations are shown in Fig. 2 for $\bar{U} = 10$. We choose to classify the trajectories into the following six types based on the region they occupy in the square cross-section (gray region in Fig. 2): (i) Central swinging motion (green) - trajectories undergoing swinging motion about the channel centerline (similar to swinging motion in cylindrical channel [16]) and confined near the center of the channel. These trajectories are confined in the cross-sectional domain $-0.25 < x, y < 0.25$. (ii) Vertical swinging motion (cyan) - trajectories undergoing swinging motion

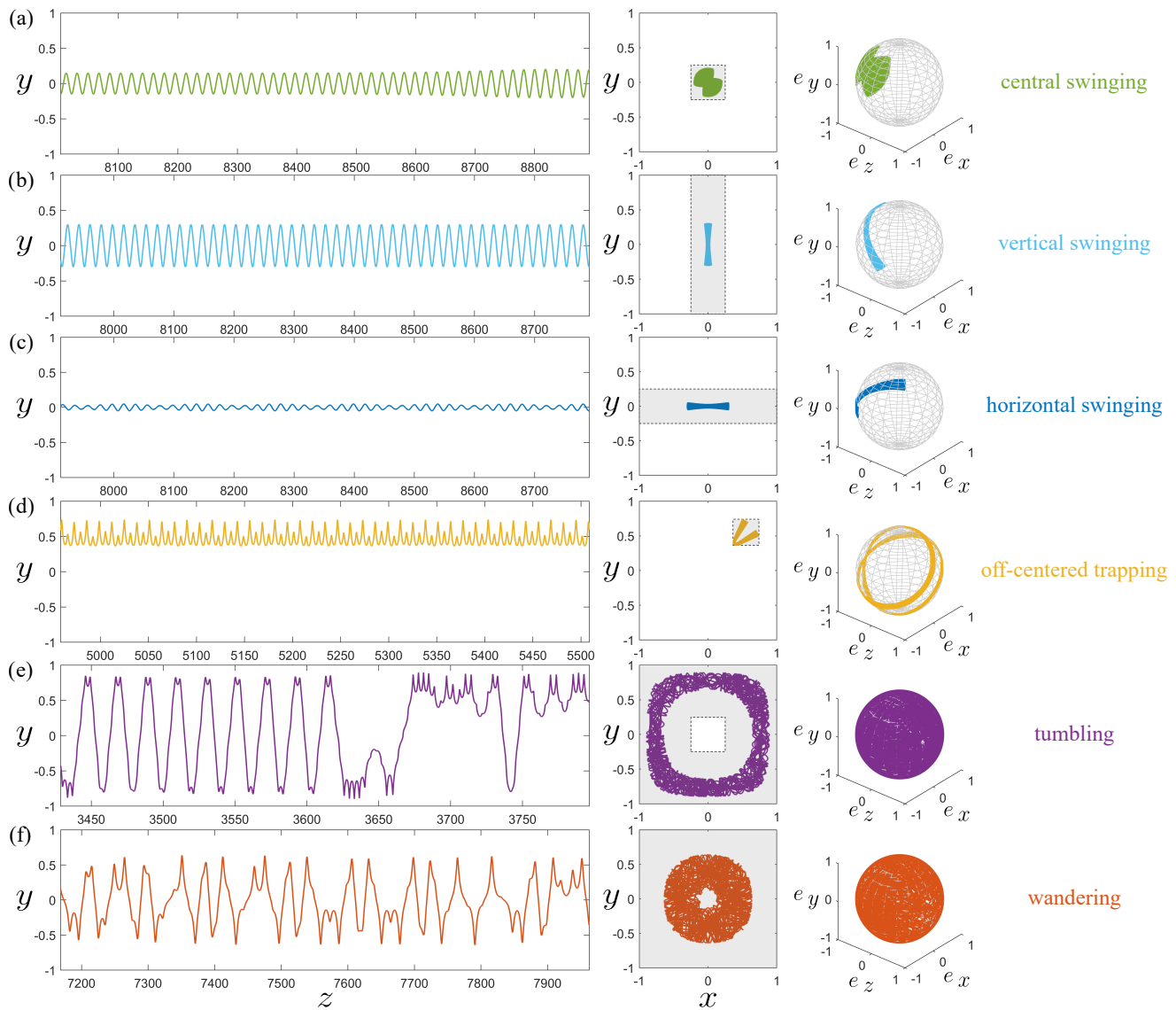


FIG. 2. Classification of active particle motion. Different trajectories of the active particle in a straight channel with square cross-section are shown in the (z, y) plane and (x, y) plane based on different initial positions for: (a) $(x(0), y(0)) = (0.15, 0.15)$, (b) $(x(0), y(0)) = (0.05, 0.30)$, (c) $(x(0), y(0)) = (0.30, 0.05)$, (d) $(x(0), y(0)) = (0.58, 0.70)$, (e) $(x(0), y(0)) = (0.75, 0.75)$ and (f) $(x(0), y(0)) = (0.55, 0.40)$. The different colors represent the classification of trajectory based on the region occupied in the cross-section. (a) Central swinging motion (green) - trajectories that stay near the center of the channel inside the gray square $-0.25 < x, y < 0.25$, (b) vertical swinging motion (cyan) - trajectories that are confined in the x direction i.e. inside the vertical band $-0.25 < x < 0.25$, (c) horizontal swinging motion (blue) - trajectories that are confined in the y direction i.e. inside the horizontal band $-0.25 < y < 0.25$, (d) off-centered trapping (yellow) - trajectories that are confined in a rectangular of area less than half the area of cross-section, and, the box crosses at most one centerline: the vertical centerline ($x = 0$) or the horizontal centerline ($y = 0$), (e) tumbling motion (purple) - trajectories that stay near the edges of the channel i.e. outside the region of central swinging motion, and (f) wandering motion (red) - trajectories that explore both the central as well as outer region of the cross-section. Other parameters were fixed to $\bar{U} = 10$, $z(0) = 0$, $\theta(0) = 0$ and $\phi(0) = 0$. See also supplemental videos S1-S6 for videos of trajectories corresponding to panels (a)-(f), respectively.

in the vertical y direction and confined in the x direction. These trajectories are confined in a vertical band with $-0.25 < x < 0.25$. (iii) Horizontal swinging motion (blue) - trajectories undergoing swinging motion in the horizontal x direction and confined in the y direction. These trajectories occupy a horizontal band with

$-0.25 < y < 0.25$. (iv) Off-centered trapping (yellow) - trajectories that are confined in a rectangular box of area less than half the area of the cross-section, and this box crosses at most one centerline but not both, i.e. the box crosses either the vertical centerline ($x = 0$) or the horizontal centerline ($y = 0$) or none. (v) Tumbling mo-

tion (purple) - trajectories that stay outside the central region and wander near the channel walls. These trajectories occupy the region in the square cross-section which is outside the central region defined for central swinging motion. (vi) Wandering motion (red) - trajectories that visits both the central region defined for central swinging motion, as well as the outer region defined for tumbling motion.

B. Comparison with cylindrical channel

For a square cross-section ($AR = 1$) we have the approximate dimensionless fluid flow field from Eq. (8),

$$\bar{u}_s(x, y) = \bar{U}(1 - x^2)(1 - y^2) = \bar{U} (1 - (x^2 + y^2) + x^2y^2).$$

By introducing the following flow field

$$\bar{u}_{cs}(x, y) = \bar{U} (1 - (x^2 + y^2) + \alpha x^2y^2),$$

we can continuously transform from a circular cross-section flow field in Eq. (10) ($\alpha = 0$) to the square cross-section flow field $\bar{u}_s(x, y)$ ($\alpha = 1$). The corresponding nonlinear ODEs for flow field $\bar{u}_{cs}(x, y)$ are:

$$\begin{aligned} \dot{x} &= -\cos \theta \sin \phi & (13) \\ \dot{y} &= \sin \theta \\ \dot{\theta} &= -\bar{U}y \cos \phi + \alpha \bar{U}x^2y \cos \phi \\ \dot{\phi} &= \bar{U}(-y \tan \theta \sin \phi + x) + \alpha \bar{U}xy(x \tan \theta \sin \phi - y). \end{aligned}$$

It can be seen from Eq. (13) that the equilibrium states and their linear stability found for a square cross-section ($AR = 1$) in Sec. III will be the same as that for a circular cross-section Zöttl and Stark [16]. This is to be expected since the additional term present in the $\dot{\theta}$ and $\dot{\phi}$ equations in (13) contributes at an order $O(\epsilon^3)$ near the equilibrium points and hence their effects are not felt at leading order i.e. $O(\epsilon)$.

For our square channel, we only have the constant of motion in Eq. (7) as

$$H_s = \frac{1}{2}\bar{U}(x^2 + y^2 - x^2y^2) + 1 - \cos \phi \cos \theta.$$

We chose $H_s = 1 + \frac{1}{2}\bar{U} + H_g \geq 0$, to better compare with H_c in Eq. (11) for a circular cross-section. Furthermore, the time derivative of the second constant of motion L_z for the cylindrical channel in Eq. (12), takes the following form for a square cross-section ($\alpha = 1$):

$$\frac{dL_z}{dt} = \bar{U}xy \cos \theta \cos \phi (x^2 - y^2). \quad (14)$$

We see that this quantity will not be varying significantly when either x or y or both are small i.e. the motion is confined either near the center of the channel or along the x or the y axis. Hence, in this regime, we expect the motion of the system to be periodic/quasiperiodic since the

system is close to the cylindrical channel system which is both Hamiltonian and integrable. Furthermore, from Eq. (14), the right-hand side will be near zero if the orientation is confined near $\theta = \pm\pi/2$ or $\phi = \pm\pi/2$ or if the motion is along diagonals $y = \pm x$. We expect our square cross-section system to deviate from a Hamiltonian integrable system when the motion takes place away from the channel center and chaos may arise. Hence, for swinging motion in the square cross-section which is confined near the center of the channel or along x or y axis, we typically expect regular (periodic/quasiperiodic) motion. Conversely, for tumbling motion that takes place away from the channel center, chaotic motion is possible. An example showing a comparison of active particle dynamics between circular and square cross-section for a typical tumbling motion with the same initial conditions $(x(0), y(0), \theta(0), \phi(0)) = (0.55, 0.58, \pi/24, \pi/24)$ is shown in supplemental video S7.

C. Motion near equilibrium states

Since the equilibrium states of the particle-fluid system are located at the center of the cross-section ($x = 0, y = 0$) and the additional nonlinear x^2y^2 term in the square channel flow field is small near these equilibrium points, we expect the motion near the equilibrium states to be similar to that of the circular cross-section [16].

The eigenvectors corresponding to eigenvalues $\lambda_{1,2} = \pm i\sqrt{\bar{U}}$ for the upstream-oriented particle equilibrium are

$$\mathbf{v}_1 = a_1 \begin{bmatrix} 1 \\ 0 \\ 0 \\ -i\sqrt{\bar{U}} \end{bmatrix} + b_1 \begin{bmatrix} 0 \\ 1 \\ i\sqrt{\bar{U}} \\ 0 \end{bmatrix}$$

and

$$\mathbf{v}_2 = a_2 \begin{bmatrix} 1 \\ 0 \\ 0 \\ i\sqrt{\bar{U}} \end{bmatrix} + b_2 \begin{bmatrix} 0 \\ 1 \\ -i\sqrt{\bar{U}} \\ 0 \end{bmatrix}$$

respectively. Here, a_1, b_1, a_2 and b_2 are complex constants with $\bar{a}_1 = a_2$ and $\bar{b}_1 = b_2$, where the overbar denotes a complex conjugate. For small perturbations around this equilibrium point, we numerically observe periodic and quasiperiodic active particle motion confined near the center of the channel (e.g. see Fig. 2(a) and supplemental video S1). We further find that the motion decouples in the (x, ϕ) and (y, θ) variables near this equilibrium point and we obtain the following system for the linearized equation of motion near this equilibrium:

$$\begin{aligned} \ddot{\theta}_1 + \bar{U}\theta_1 &= 0, \\ \dot{y}_1 &= \theta_1, \\ \ddot{\phi}_1 + \bar{U}\phi_1 &= 0, \\ \dot{x}_1 &= -\phi_1. \end{aligned}$$

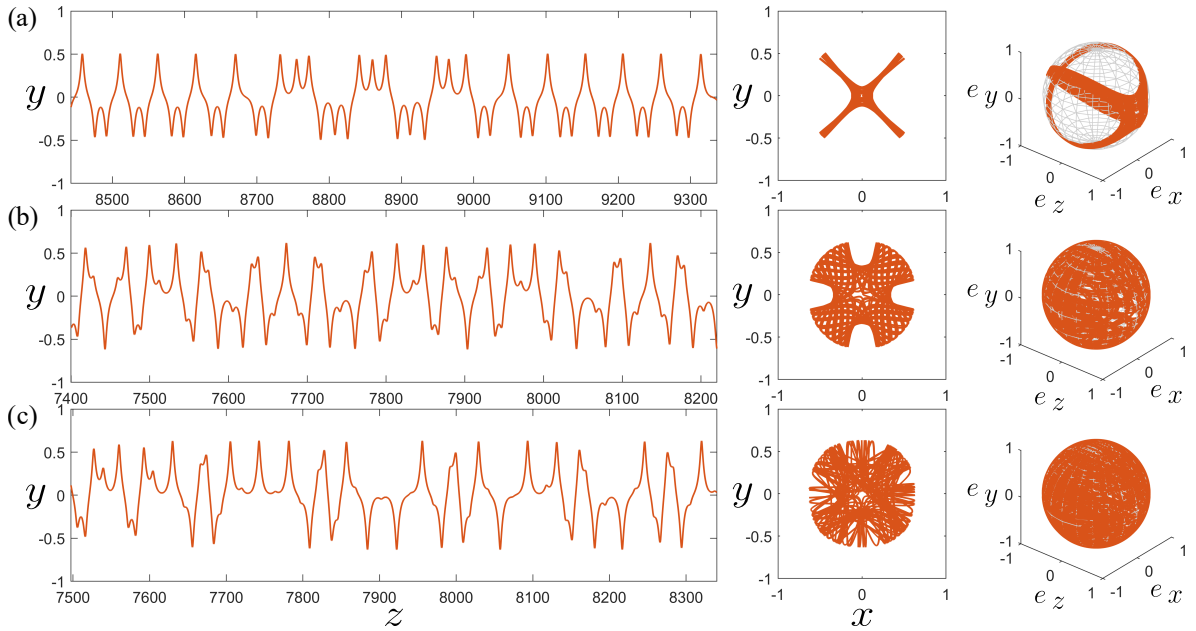


FIG. 3. Active particle motion for small perturbations near the unstable saddle equilibrium. Different trajectories of the active particles in the (z, y) plane and (x, y) plane for small perturbations: (a) in the direction of the unstable manifold $(x(0), y(0), \theta(0), \phi(0)) = (0, 0, 0, \pi) + (0.02, 0.02, 0.02\sqrt{U}, 0.02\sqrt{U})$, (b) in the direction of the stable manifold $(x(0), y(0), \theta(0), \phi(0)) = (0, 0, 0, \pi) + (0.02, 0.02, -0.02\sqrt{U}, -0.02\sqrt{U})$ and (c) small general perturbations $(x(0), y(0), \theta(0), \phi(0)) = (0, 0, 0, \pi) + (0.01, 0.02, 0.015, -0.005)$. The parameter $U = 10$ was fixed and $z(0) = 0$. See also supplemental videos S8-S10 for videos of panels (a)-(c), respectively.

Thus, the evolution of active particle orientations θ and ϕ follow simple harmonic motion with oscillating frequency \sqrt{U} and these oscillating orientations drive the translational motion of the active particle near this equilibrium point. Hence, the response to general small perturbations around this equilibrium point is a superposition of the above two decoupled oscillatory motions.

The eigenvectors with eigenvalues $\lambda_{3,4} = \pm\sqrt{U}$ for the downstream-oriented equilibrium point are

$$\mathbf{v}_3 = a_3 \begin{bmatrix} 1 \\ 0 \\ 0 \\ \sqrt{U} \end{bmatrix} + b_3 \begin{bmatrix} 0 \\ 1 \\ \sqrt{U} \\ 0 \end{bmatrix}$$

and

$$\mathbf{v}_4 = a_4 \begin{bmatrix} 1 \\ 0 \\ 0 \\ -\sqrt{U} \end{bmatrix} + b_4 \begin{bmatrix} 0 \\ 1 \\ -\sqrt{U} \\ 0 \end{bmatrix}$$

respectively, with real constants a_3, b_3, a_4 and b_4 . This equilibrium is a saddle point with its unstable manifold tangent to the hyperplane spanned by the two vectors of \mathbf{v}_3 while its stable manifold is tangent to the hyperplane spanned by the two vectors of \mathbf{v}_4 . To understand the nature of trajectories with small perturbations around this equilibrium point, we simulate motion with different initial perturbations. Some typical trajectories starting

near this unstable equilibrium are shown in Fig. 3 with perturbations in the direction of stable/unstable manifolds as well as general perturbation. We see that for a perturbation in the direction of the unstable manifold of the saddle, Fig. 3(a) and supplemental video S8, we obtain a cross-shaped trajectory in the channel cross-section that switches aperiodically between the four diagonals. The chaos here appears to be low-dimensional since the trajectory executes well-defined path on the cross-shape with unpredictability only in the selection of the branches it traverses. For a perturbation in the direction of the stable manifold, Fig. 3(b) and supplemental video S9, we obtain a fan-shaped apparently quasiperiodic trajectory, while for a general perturbation as shown in Fig. 3(c) and supplemental video S10, we obtain a chaotic trajectory with no clear structure. In all cases, we find that small perturbation from this unstable saddle equilibrium leads to wandering-type trajectories that go away from this equilibrium state and explore both the inner and outer regions of the square cross-section.

D. Parameter space exploration

We have observed that both the initial conditions and the system parameters can greatly influence the type of active particle trajectory that is realized based on the classification of trajectories described in Fig. 2. In this section, we explore the effects of the initial position and

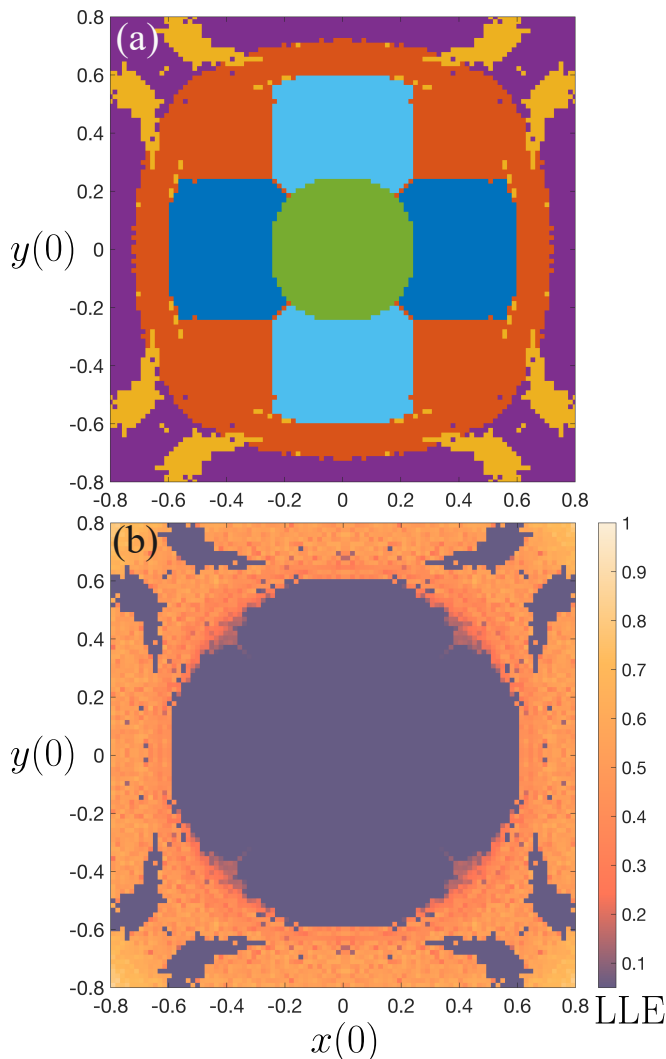


FIG. 4. (a) Classification of active particle trajectories and (b) largest Lyapunov exponent (LLE) in the initial position $(x(0), y(0))$ plane for the types of trajectories shown in Fig. 2 with fixed $\bar{U} = 10$, $\theta(0) = 0$ and $\phi(0) = 0$. Green (●) is central swinging motion, cyan (●) is vertical swinging motion, blue (●) is horizontal swinging motion, yellow (●) is off-centered trapping motion, purple (●) is tumbling motion and red (●) is wandering motion.

orientation, as well as the parameter \bar{U} on the active particle motion.

1. Effect of initial position

The active particle dynamics are described by the 4D nonlinear dynamical system in Eq. (9) which require four initial conditions: two position co-ordinates $x(0)$ and $y(0)$, and two orientation angles $\theta(0)$ and $\phi(0)$. Since there are four initial conditions, we fixed two of them and explore the types of active particle trajectories realized in the initial-condition plane formed by the re-

maining two initial conditions. We fix the orientation of the active particle to the upstream equilibrium state i.e. $\theta(0) = 0$, $\phi(0) = 0$, and explore the active particle trajectories in the $(x(0), y(0))$ plane. We consider initial positions restricted to the domain $x, y \in [-0.8, 0.8]$. This is done to exclude trajectories that get too close to the wall where interactions of the active particle with the wall may become important. A typical plot at $\bar{U} = 10$ depicting the classification of trajectories realized for different initial positions in the cross-section is shown in Fig. 4(a). We find that initial positions near the center of the channel keeps the motion confined near the center of the channel as shown by the green region for central swinging motion (see Fig. 2(a)). An active particle starting out further away from the center of the channel in the vertical and horizontal directions, remains confined in these directions and we observe cyan and blue regions corresponding to vertical swinging and horizontal swinging motion, respectively (see Fig. 2(b)-(c)). Along the diagonals and/or beyond the central region, we have a red region corresponding to wandering trajectories (see Fig. 2(f)). Near the edges of the square cross-section, we have a purple region corresponding to tumbling trajectories (see Fig. 2(e)). Lastly, near the corners, we see islands of yellow regions in the sea of purple corresponding to off-centered confined motion (see Fig. 2(d)).

The above trajectory classification in the initial-condition space is based on the region occupied by the trajectory in the cross-section and does not necessarily capture information about the regular (periodic/quasiperiodic) or chaotic nature of trajectories. However, we typically find that trajectories which are confined near the center of the channel exhibit regular motion whereas active particles that travel near the edges of the cross-section show aperiodic motion and hints of chaos. Furthermore, the trajectories that travel near the edges can flip its sense of rotation in the cross-section between clockwise and counterclockwise (e.g. see tumbling trajectory in supplemental video S5 and S7). The presence of chaos in these trajectories can be quantified by calculating the largest Lyapunov exponent (LLE) of the underlying nonlinear dynamical system [25]. If the LLE is zero, then the active particle motion is either periodic or quasiperiodic, whereas a positive LLE indicates chaos (with the degree of sensitivity to initial conditions given by the magnitude of LLE). We plot the LLE in the plane of initial conditions $(x(0), y(0))$ in Fig 4(b) for the same parameter values as Fig 4(a). We typically find that particles starting in the central region of the square cross-section have regular motion, whereas particles starting near the edges (outer red region and purple region) of the channel are chaotic. However, we also find anomalous periodic regions near corners (within the chaotic sea) where a particle starting in these small regions near the corners of the channel can show regular dynamics. These anomalous periodic regions correspond to the yellow region in Fig. 4(a) indicating off-centered trapping motion.

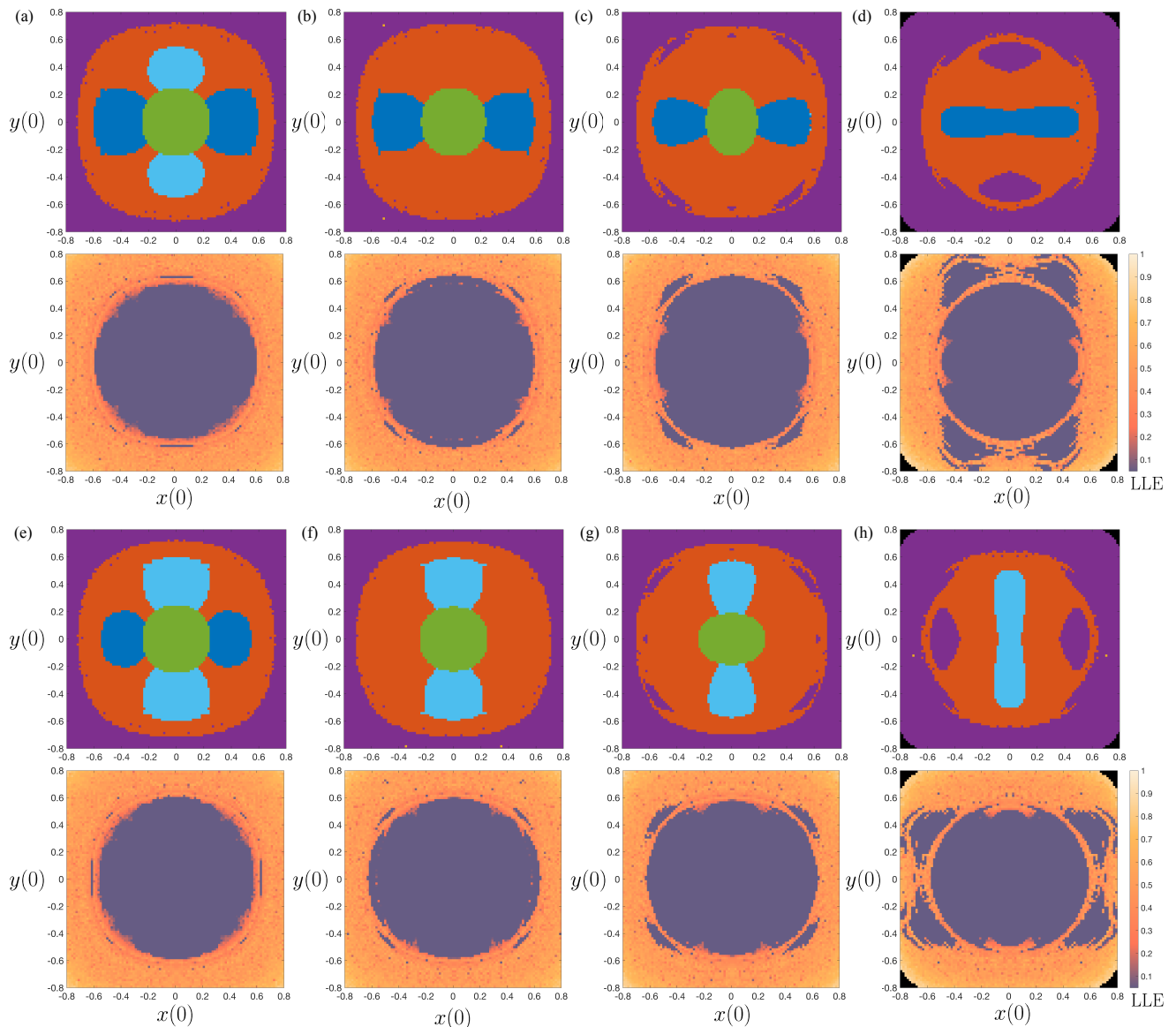


FIG. 5. Trajectory classification (top panels) and LLE (bottom panels) in the initial position $(x(0), y(0))$ plane for fixed $\bar{U} = 10$ and varying initial orientations $\theta(0)$ and $\phi(0)$. For fixed $\theta(0) = 0$ and (a) $\phi(0) = \pi/24$, (b) $\phi(0) = \pi/12$, (c) $\phi(0) = \pi/6$ and (d) $\phi(0) = \pi/3$. For fixed $\phi(0) = 0$ and (e) $\theta(0) = \pi/24$, (f) $\theta(0) = \pi/12$, (g) $\theta(0) = \pi/6$ and (h) $\theta(0) = \pi/3$. Green (●) is central swinging motion, cyan (●) is vertical swinging motion, blue (●) is horizontal swinging motion, purple (●) is tumbling motion and red (●) is wandering motion. Black regions in panels (d) and (h) correspond to trajectories that came too close to the channel walls i.e. trajectories that went outside a square of $[-0.95, 0.95] \times [-0.95, 0.95]$.

2. Effect of initial orientation

We now explore how the classification regions occupied by different types of trajectories in the $(x(0), y(0))$ initial position plane vary with changes in the initial orientation angles $\theta(0)$ and $\phi(0)$ of the active particle around the upstream-oriented equilibrium.

First, we explore the effects of variations in $\phi(0)$ for fixed $\theta(0) = 0$. For a small positive value of $\phi(0) = \pi/24$, we find that the blue and cyan regions shrink marginally (see top panel of Fig. 5(a)) compared to the $\phi(0) = 0$ case (see Fig. 4(a)). Further increasing to

$\phi(0) = \pi/12$, we find that cyan region corresponding to vertically swinging motion vanishes as shown in Fig. 5(b). This is because the value of $\phi(0)$ is no longer close to its upstream equilibrium and hence the larger initial value of $\phi(0)$ are unable to maintain vertical swinging motion of the active particle. Further increasing $\phi(0)$ leads to the shrinkage and disappearance of the green region for central swinging motion too (see Fig. 5(c)-(d)). Again the large value of $\phi(0)$ is unable to maintain a confined trajectory near the channel center. Further, we see that the purple region, corresponding to trajectories confined near the edges, starts mixing with the red region and leads to

shrinking of the red region. In terms of the chaotic nature of the trajectories, we see from the bottom panels of Fig. 5(a)-(d), the regular region progressively increases with increasing $\phi(0)$ as a vertical band around the central region of the channel. However, structure indicating chaotic motion also persists within this vertical band of regular motion. The black region near the corners for Fig. 5(d) corresponds to trajectories that were too close to the channel walls i.e. trajectories that went outside the square domain $(x, y) \in [-0.95, 0.95] \times [-0.95, 0.95]$.

We see a similar trend for variations in $\theta(0)$ for fixed $\phi(0) = 0$ with the blue regions replaced with cyan regions. The blue and green regions disappear for large $\theta(0)$ since larger values of $\theta(0)$ cannot give rise to a horizontally swinging motion and trajectories confined to the central region, respectively.

We note that the yellow periodic islands present near the corner of the square cross-section in Fig. 4(a) disappear for variations with initial orientation angle when the other initial orientation angle is kept fixed to zero as shown in Fig. 5. However, similar to cyan/blue regions in Fig. 5(a-d)/(e-h), there does exist a non-zero volume in the initial-condition space where yellow regions would also persist for small variations in $\phi(0)$ and $\theta(0)$ from the upstream equilibrium state.

3. Effect of \bar{U}

We now look at variations in active particle dynamics with respect to the dimensionless parameter \bar{U} - ratio of the maximum flow speed to the intrinsic active particle speed. For $\bar{U} \ll 1$, the active particle intrinsic velocity dominates the flow field and hence, the particle will readily encounter the walls. Moreover, the active particle's self-generated flow fields would need to be captured to understand its dynamics. Since the simple model used in this work does not capture these effects, we do not explore this regime. This regime of active particle motion in a quiescent fluid within a rectangular duct has been recently explored in detail numerically by Radhakrishnan *et al.* [26]. Figure 6 shows the different types of trajectories (left panels) and LLE (right panels) in the initial position space for various values of \bar{U} and fixed initial upstream orientation $\theta(0) = 0$ and $\phi(0) = 0$. For $\bar{U} \lesssim 1$, as shown in Fig. 6(a), we observe regular swinging motion of the active particle about the channel center with the net migration of the particle upstream along the channel. For $\bar{U} \gtrsim 1$, as shown in Fig. 6(b), we again observe regular swinging motion but now the net migration of the particle is downstream along the channel. Increasing to $\bar{U} = 5$, the types of trajectories do not change qualitatively compared to Fig. 6(a)-(b), but we start seeing the emergence of chaotic motion near the corners of the channel cross-section as shown in Fig. 6(c). Further increase in \bar{U} to 7.5 we see the emergence of purple regions near the edges of the cross-section and we also see an increase in the extent of chaotic regions

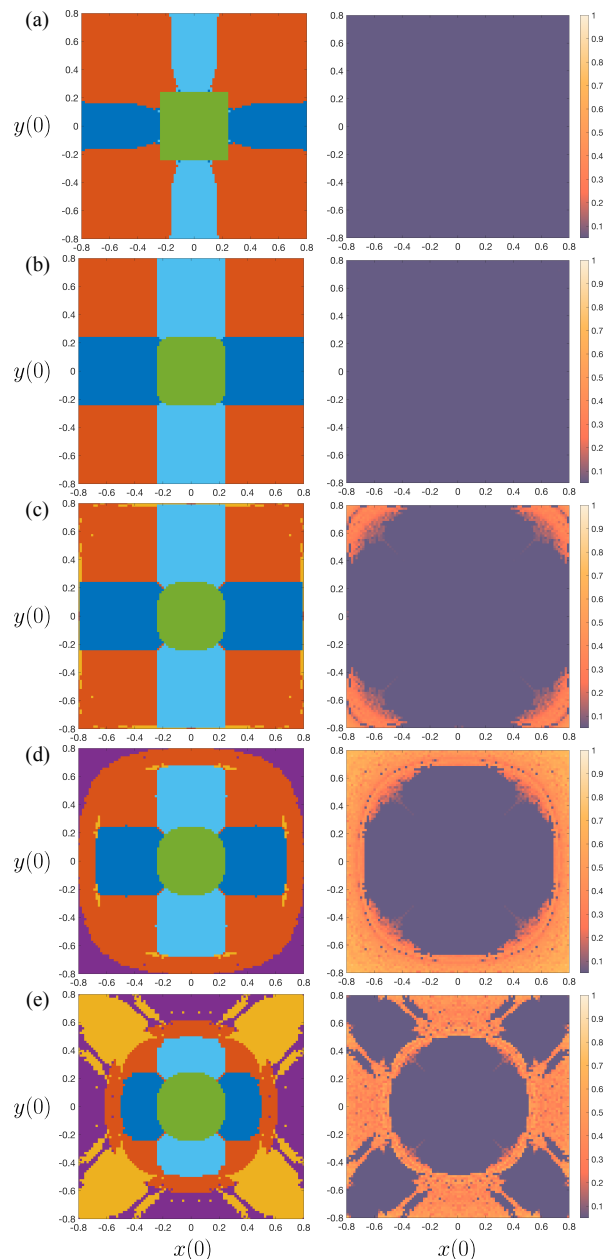


FIG. 6. Trajectory classification (left panels) and LLE (right panels) in the initial position $(x(0), y(0))$ plane for the types of trajectories shown in Fig. 2 and different values of \bar{U} : (a) $\bar{U} = 0.5$, (b) $\bar{U} = 2.5$, (c) $\bar{U} = 5$, (d) $\bar{U} = 7.5$ and (e) $\bar{U} = 15$. Initial orientation angles are fixed to $\theta(0) = 0$ and $\phi(0) = 0$. Green (●) is central swinging motion, cyan (●) is vertical swinging motion, blue (●) is horizontal swinging motion, yellow (●) is off-centered trapping motion, purple (●) is tumbling motion and red (●) is wandering motion.

towards the center of the channel (see Fig. 6(d)). For a large value of $\bar{U} = 15$, we see the appearance of regular trajectories in the yellow regions near the corners of the channel cross-section. Hence, for the parameter values and the range of \bar{U} values shown in Fig. 6, we find that as \bar{U} increases, the green region corresponding to central

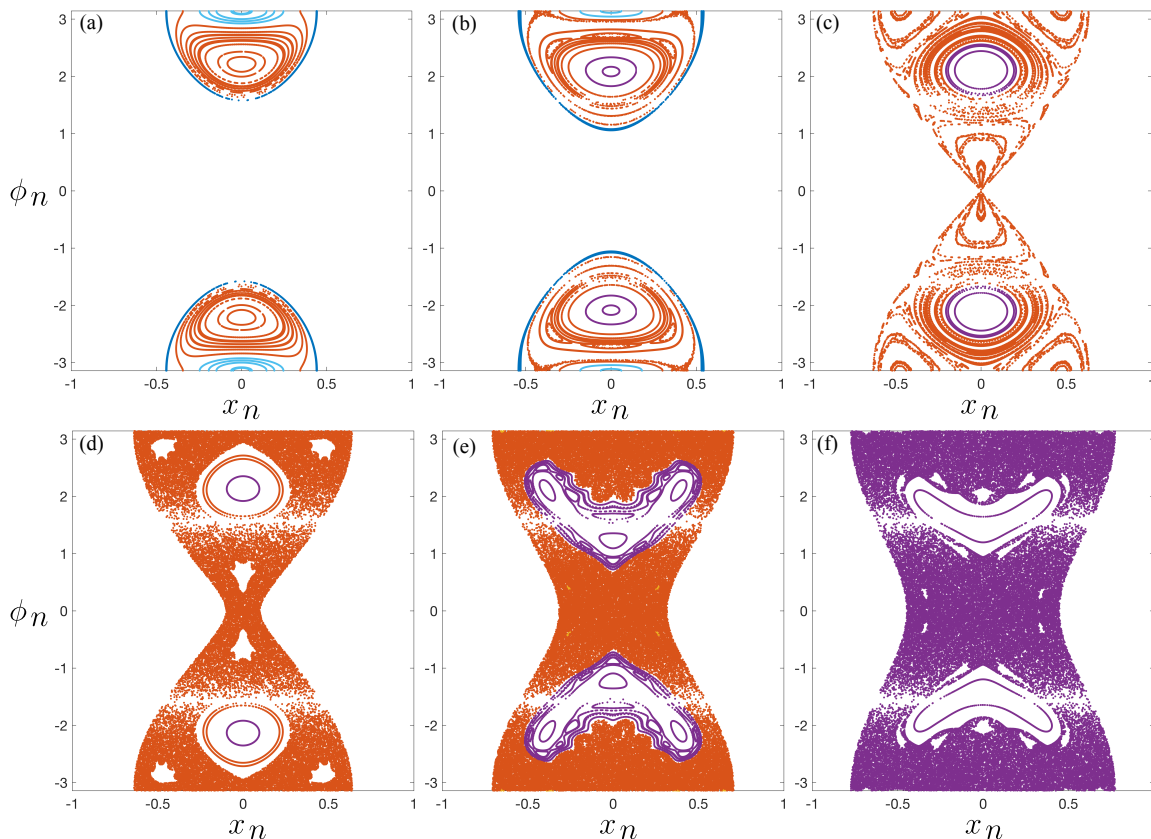


FIG. 7. Poincaré maps in the (x_n, ϕ_n) plane for $\theta(t_n) = 0$ ($\dot{\theta}(t_n) > 0$) and (a) $H_s = 1$, (b) $H_s = 1.5$, (c) $H_s = 2$, (d) $H_s = 2.05$, (e) $H_s = 2.5$ and (f) $H_s = 3$. The parameter $\bar{U} = 10$ was fixed and the initial conditions were chosen based on Eq. (15) to keep H_s fixed. Cyan (●) is vertical swinging motion, blue (●) is horizontal swinging motion, purple (●) is tumbling motion and red (●) is wandering motion.

swinging motion does not change significantly while the cyan and blue region for vertical and horizontal swinging shrink progressively. Further, with increasing \bar{U} , the red region of wandering motion also shrinks with the appearance of tumbling and off-centered trapping motion near the edges and corners of the cross-section. In terms of the chaotic nature, we see a progressive increase in chaotic trajectories up to $\bar{U} = 7.5$, but any further increase in \bar{U} leads to the appearance of regions of regular motion near the corners.

4. Poincaré map and sticky trajectories

Since there exists one constant of motion H_s for our 4D dynamical system in Eq. (9), the effective dynamics of the system take place in 3D. We can further explore the nature of the system dynamics and transition to chaos by using Poincaré sections which allows us to visualize regular and chaotic regions of the system on a 2D plot. We obtain a Poincaré map by sampling the active particle trajectory at times t_n that correspond to the intersection of the phase-space trajectory with the $\theta = 0$ (equivalently $e_y = 0$) hyperplane, i.e. $\theta(t_n) = 0$

with $\dot{\theta}(t_n) > 0$. At these times t_n , we store the values $\phi_n = \phi(t_n)$ and $x_n = x(t_n)$, and plot them against each other giving us a Poincaré map. We repeat this for active particle trajectories with different initial conditions but for a fixed value of the constant of motion H_s i.e. the initial conditions satisfy

$$H_s = \frac{1}{2} \bar{U} (x(0)^2 + y(0)^2 - x^2(0)y^2(0)) + 1 - \cos(\phi(0)) \cos(\theta(0)). \quad (15)$$

In this way, we obtain Poincaré maps as shown in Fig. 7 for different values of the constant of motion H_s . We find that for small values of H_s , we observe regular behavior with ubiquitous quasiperiodic trajectories that correspond to closed curves on the Poincaré map (see Fig. 7(a)-(b)). As H_s is increased, we observe that, due to nonlinear resonances, some of these orbits break into a chain of smaller orbits (see Fig. 7(c)). Further increase in H_s gives rise to chaos as evident by the apparently random scatter of points in the Poincaré map (see Fig. 7(d)-(e)). At these large values of H_s , we have a mixture of order and chaos where small islands of regular behaviors exist within the chaotic sea. Increase in the value of H_s can also be interpreted as initial positions going away

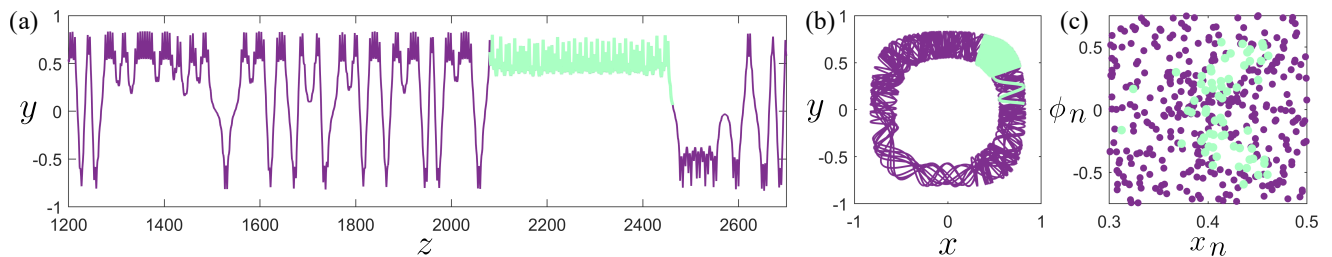


FIG. 8. Sticky trajectory for active particle in a square cross-section. Particle trajectory in the (a) (z, y) plane and (b) (x, y) plane, as well as (c) Poincaré map in the (x_n, ϕ_n) plane for $\theta = 0$ ($\dot{\theta} > 0$). Purple shows the entire trajectory of the particle while light green shows a typical “sticky” region for the trajectory. The parameter $\bar{U} = 10$ and initial conditions were chosen such that $H_s = 3.5$ with $x(0) \approx 0.6861$, $y(0) \approx 0.6582$, $z(0) = 0$, $\theta(0) = 0$ and $\phi(0) = 0$. See also supplemental video S11 for a video of the trajectory.

from the center of the channel. For fixed upstream initial orientation $\theta(0) = 0$, $\phi(0) = 0$, Eq. (15) describes a closed curve

$$x(0)^2 + y(0)^2 - x^2(0)y^2(0) = 2H_s/\bar{U}.$$

These closed curves are the same shape as the contours of the flow field $\bar{u}(x, y)$. Small values of H_s correspond to circle-like closed curves near the center of the channel while increasing H_s leads to square-like closed curves away from the center of the channel. Since near the center of the channel, the dynamics of the system are similar to a circular cross-section and hence integrable, this transition to chaos with increasing H_s maybe understood in terms of the theory of nearly integrable Hamiltonian systems and KAM theory [27].

When islands of regular behaviors exist within the chaotic sea of a Poincaré map, “sticky” trajectories can arise where a long time is spent in the vicinity of these periodic islands [28]. An example of such a sticky tumbling trajectory is shown in Fig. 8 and supplemental video S11. In this plot, panels (a) and (b) show the trajectory in different planes while panel (c) shows a Poincaré map with the light green colored part in all three panels representing the “sticky” behavior. Such trajectories spend a very long time near the boundaries of the periodic islands compared to the time spent in a domain of chaotic sea of the same phase-space volume.

5. Dynamics in the large \bar{U} limit

In the limit of large $\bar{U} \gg 1$, Eq. (9) approach a singular limit for the evolution of θ and ϕ . Hence, to understand this regime, we rescale the dimensionless time by \bar{U} in Eq. (9) (with $AR = 1$) and obtain the following system:

$$\begin{aligned} \dot{x} &= -\frac{1}{\bar{U}} \cos \theta \sin \phi & (16) \\ \dot{y} &= \frac{1}{\bar{U}} \sin \theta \\ \dot{\theta} &= -y \cos \phi (1 - x^2) \\ \dot{\phi} &= -y \tan \theta \sin \phi (1 - x^2) + x(1 - y^2). \end{aligned}$$

This form of the system removes the singular terms and allows efficient numerical solution. A typical classification of trajectories at a large value of $\bar{U} = 50$ along with an example trajectory and Poincaré maps is shown in Fig. 9. In this regime of large \bar{U} we find that chaos ceases and we have regular behaviors. A typical regular trajectory that confines itself to a section of the channel is shown in Fig. 9(a). Simulating many different initial conditions with fixed initial upstream orientation $\theta(0) = 0$ and $\phi(0) = 0$ gives us the classification in the initial position plane $(x(0), y(0))$ as shown in Fig. 9(b). Compared to Fig. 6, we find that the central green region still exists while the cyan, blue and red regions have almost vanished. Outside the central region, the behavior is dominated by off-centered trapped trajectories. Two different Poincaré maps at $H_s = 1.75$ and $H_s = 3$ are shown in Figs. 9(c) and (d) respectively. These typically show closed loops indicating quasiperiodic behavior of the system in this regime. With variation in the initial orientation angles $\theta(0)$ and $\phi(0)$ from the upstream equilibrium state, we find that in the initial position plane, some yellow regions transition to purple regions corresponding to regular tumbling trajectories.

Hence, from Figs. 6 and 9 we see that the active particle motion is regular for small and large \bar{U} , whereas chaos emerges for intermediate \bar{U} .

E. Active particle transport along the channel

The trajectories shown in Fig. 2 started at $z = 0$ and the time series is shown for $t = 900$ to $t = 1000$. We see that the transport of the active particle along the z direction i.e. along with the flow, can vary significantly depending on the type of active particle motion realized in the channel cross-section. Active particles that perform swinging motion near the center of the channel (e.g. green, blue, cyan and some red trajectories) will travel further along the channel compared to active particles whose motion is confined near the edges of the cross-section (e.g. purple trajectory). Figure 10 shows for different \bar{U} values, a contour plot of the z location at the end

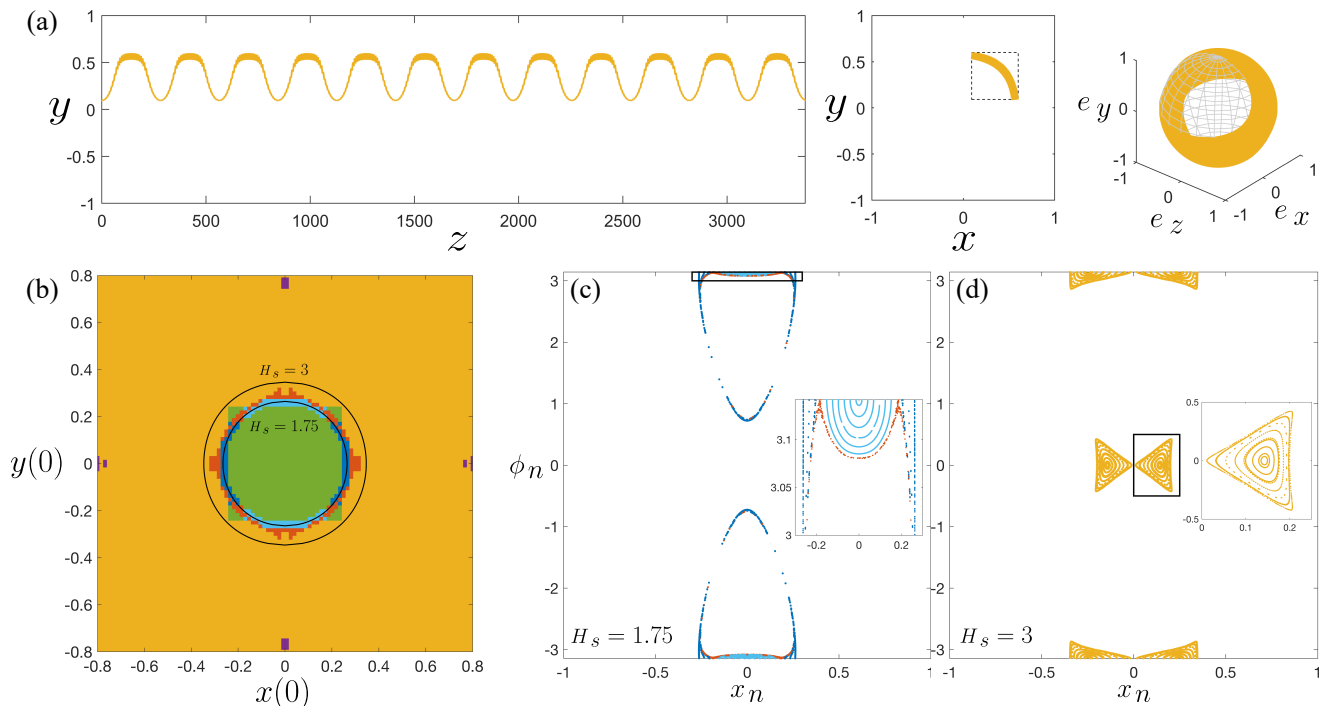


FIG. 9. Active particle dynamics for large $\bar{U} = 50$ starting at $z(0) = 0$ with fixed initial upstream orientation angles $\theta(0) = 0$ and $\phi(0) = 0$. (a) A typical confined trajectory in the (z, y) (left) and (x, y) (middle) plane, as well as the orientation evolution (right) for initial position $x(0) = 0.6, y(0) = 0.1$. (b) Classification of behaviors in the $(x(0), y(0))$ initial position plane using the color scheme in Fig. 2. Poincaré maps in the (x_n, ϕ_n) plane for $\theta(t_n) = 0$ with $\dot{\theta}(t_n) > 0$ for the constant of motion (c) $H_s = 1.75$ and (d) $H_s = 3$. These values of constant of motion are indicated by black curves in panel (b). The trajectory in panel (a) was simulated for $t = 100$ in the same units as Eq. (9), which corresponds to $t = 100\bar{U}$ in the units of Eq. (16). See also supplemental videos S12 for a video of the active particle trajectory in panel (a).

of the simulation ($t = 1000$) in the $(x(0), y(0))$ plane for initially upstream-oriented active particles (starting from $z = 0$). For a small value of $\bar{U} = 0.5$, we see that the final z positions are negative indicating that the active particle's intrinsic speed dominates the fluid flow speed resulting in a net upstream migration of the active particle. For a larger value of $\bar{U} = 2.5$, the fluid speed dominates particle speed and we obtain a net downstream migration of all active particles. Further increase to $\bar{U} = 5$ does not change the transport profile near the center of the cross-section, however, near the corners, we see fluctuations in the transport profile due to the appearance of chaotic wandering motion in this region (see Fig. 6(c)). For larger values of \bar{U} the active particle transport is dominated by the background fluid flow profile. We find a central plug region corresponding to large transport of the active particles undergoing swinging motion near the center of the channel where flow speed is large, while near the edges and corners we observe small transport of active particle corresponding to off-centered trapping or tumbling trajectories that stay near the outer regions of the cross-section where the flow speed is small. In between the large transport central plug region and the small transport outer region, we observe some fluctuations in the transport contours that correspond to chaotic wandering trajectories.

VI. DYNAMICS IN WIDER RECTANGULAR CHANNELS

In this section, we briefly explore the effects of aspect ratio AR of the rectangular cross-section on the active particle dynamics. To understand this, we plot the trajectory classification and LLE in the initial condition plane $(x(0), y(0))$ for two different rectangular cross-sections with $AR = 2$ and $AR = 4$ as shown in Fig. 11(a) and (b) respectively, while keeping $\theta(0) = 0, \phi(0) = 0$ and $\bar{U} = 10$ fixed. We note that the classification criteria presented for square channels in Sec. V A has been scaled based on AR in the x direction for rectangular channels. So, for example, the classification of central swinging motion (green) has been modified to confinement in a rectangular box of domain $-0.25 AR < x < 0.25 AR$ and $-0.25 < y < 0.25$. For the rectangular cross-section with $AR = 2$, we find similar types of active particle trajectories at similar initial positions compared to the $AR = 1$ square channel (see Fig. 4) with some minor differences. Near the center of the channel, we obtain central swinging motion (green) as well as vertical (cyan) and horizontal (blue) swinging motion. We do see a horizontal stretching of these regions due to widening of the channel. Moreover, the relative frequency of oscillations in the horizontal and vertical direction near the center

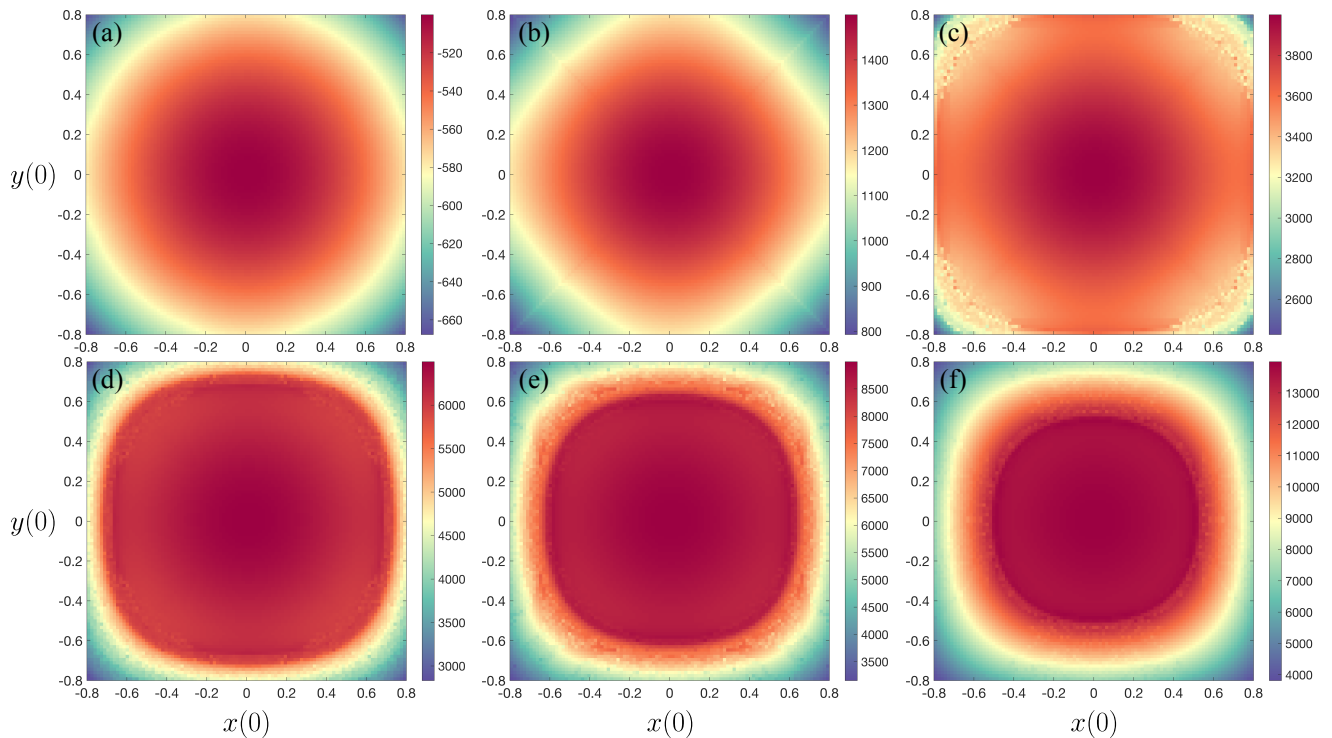


FIG. 10. Transport of the active particle along the straight channel based on the initial position in the $(x(0), y(0))$ plane for various \bar{U} and fixed $\theta(0) = 0$ and $\phi(0) = 0$. Final position of the active particle in the z direction starting at $z(0) = 0$ (color) for values of (a) $\bar{U} = 0.5$, (b) $\bar{U} = 2.5$, (c) $\bar{U} = 5$, (d) $\bar{U} = 7.5$, (e) $\bar{U} = 10$ and (f) $\bar{U} = 15$.

of the channel will be scaled by AR as per the eigenvalues in Sec. III 1. Beyond the central region, we find wandering motion (red) and tumbling motion (purple) similar to the square channel. We find that the yellow islands, corresponding to confined trajectories away from the channel center, have diminished in size compared to the square cross-section, and these regions are more scattered. A typical trajectory in the yellow region is shown in Fig. 11(c) where the motion is trapped in an off-centered vertical band compared to the motion confined near the corner for a square cross-section (see Fig. 2(d)). For the $AR = 2$ channel, we also see the emergence of small horizontal swinging (blue) regions appearing near the left and right edges of the horizontal centerline that were not present for square channels. The LLE also shows similar structure with regular trajectories near the central region of the channel and the dominance of chaos in the outer regions of the channel. The $AR = 4$ rectangular cross-section shows similar features as the $AR = 2$ channel with a few noteworthy differences. The yellow regions for off-centered trapping motion increases in extent while the small regions for horizontal swinging present for $AR = 2$ channel no longer exist. Moreover, the tumbling motion (purple) region penetrates the wandering motion (red) region near the left and right edges of the cross-section. We also note that our simple flow field approximation in Eq. (8) will become poor near the left and right edges of the cross-section with increasing AR , and hence a more accurate flow field for Poiseuille

flow in rectangular channels may be needed to accurately capture the active particle dynamics in these regions.

VII. CONCLUSIONS

In summary, we identified a general constant of motion for a point-like active particle interacting with a steady unidirectional fluid flow. We studied in detail, theoretically and numerically, the specific case of an active particle in Poiseuille flow through straight channels with rectangular cross-section. The equations of motion resulted in a 4D nonlinear dynamical system with one constant of motion. We identified two equilibrium states for this particle-fluid system located at the center of the rectangular cross-section: (i) an upstream-oriented marginally stable equilibrium where small perturbations lead to oscillatory motion about this equilibrium point and (ii) a downstream-oriented unstable saddle equilibrium. By numerically solving the system, we observed a variety of active particle trajectories for different values of \bar{U} and AR , as well as different initial conditions. These were classified based on the regions they occupy in the channel cross-section. Swinging trajectories such as central swinging, vertical swinging and horizontal swinging are typically observed as quasiperiodic motion about the center of the channel, where as off-centered trapping motion typically occurs as confined quasiperiodic motion

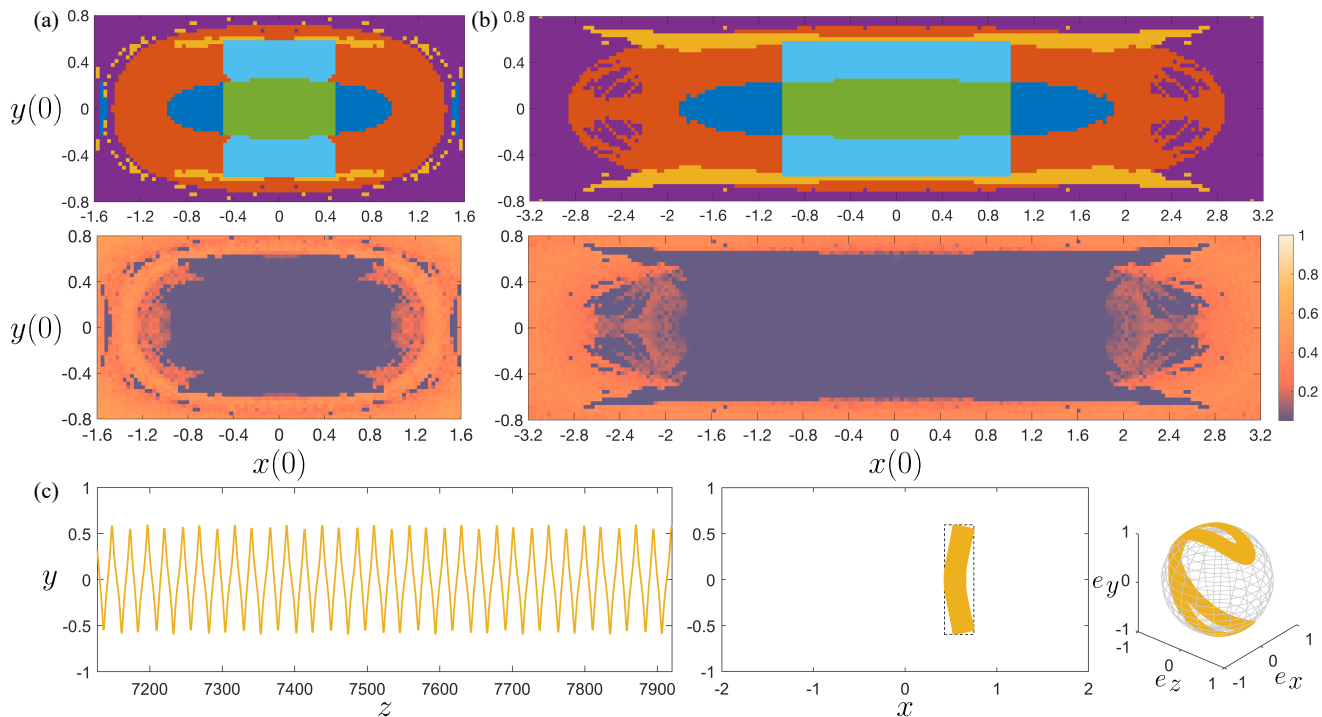


FIG. 11. Active particle trajectory classification (top) and LLE (bottom) in the initial position plane $(x(0), y(0))$ for motion in rectangular channels with (a) $AR = 2$ and (b) $AR = 4$. (c) A trajectory of a typical yellow region with $x(0) = 0.75$ and $y(0) = 0.55$ for $AR = 2$ channel. Other parameters are fixed to $\bar{U} = 10$, $z(0) = 0$, $\theta(0) = 0$ and $\phi(0) = 0$. See supplemental video S13 for a video of the active particle trajectory in panel (c).

away from the channel centerline. Tumbling trajectories stay near the edges of the cross-section while wandering trajectories visited both the central and the outer regions of the cross-section. By calculating the largest Lyapunov exponents, many of the tumbling and wandering trajectories were shown to be chaotic. Poincaré maps with increasing value of the constant of motion showed the transition to chaotic behavior and the persistence of small islands of regular behavior in the chaotic sea. This resulted in “stickiness” for chaotic tumbling trajectories where the chaotic trajectory gets trapped near a periodic state for a long time.

We studied how the active particle motion varies with the system parameters and initial conditions. With changing aspect ratio AR of the channel, we obtain the same qualitative types of trajectories. For variations with \bar{U} , we observe rich dynamics with non-chaotic motion at very small and large \bar{U} whereas chaos emerges in an intermediate range of \bar{U} . In this regime of \bar{U} where chaos arises, we found that the active particle trajectories are generally very sensitive to initial conditions with a couple of robust regimes. The active particle oriented upstream and starting near the channel center typically undergoes regular swinging motion that is robust with small variations in the initial position and orientation. Similarly, the active particle oriented upstream and starting near the edges of the channel typically undergoes chaotic tumbling motion which is again robust with small variations

of the initial conditions.

The model used in this paper is simple and can be extended in various ways to more accurately capture the motion of natural and artificial microswimmers in channel flows. The present model does not capture the interaction of the active particle with the channel walls and it would be useful to explore the effects of wall interactions to (i) understand motion of active particle in narrow channels and (ii) more accurately captures the active particle trajectories get too close to the channel walls. The present work highlights the important of initial conditions on active particle motion and hence it would be useful to perform careful microfluidic experiments with active particle to quantify the effects of initial conditions on the active particle motion in channel flows. By considering wall interactions using squirmer models for the active particle in 2D planar Poiseuille flow, Zöttl and Stark [16] showed that adding wall interactions results in emergence of dissipative dynamical features such as a stable point attractor and limit cycle attractor for the upstream-orientation swinging motion. Choudhary *et al.* [20] explored the effects of adding fluid inertia for active particles in 2D planar Poiseuille flow and reported similar dynamical features. Our previous work on the dynamics of passive spheres in 3D channel flows with non-zero fluid inertia has revealed rich dynamical structure for inertial particle focusing behaviors [29–31]. In future work, we aim to understand the effects of inertia on the dynamics

and focusing of active particle in 3D microfluidic channel flows.

ACKNOWLEDGMENTS

This research is supported under the Australian Research Council's Discovery Projects funding scheme (project number DP200100834). Some of the results were computed using supercomputing resources provided by the Phoenix HPC service at the University of Adelaide.

Appendix A: Calculation for general constant of motion

For dynamics of the active particle suspended in a unidirectional flow field $\bar{u}(x, y)$ as given by Eqs. (3), we show that following is a constant of motion:

$$H_g = -\frac{1}{2}\bar{u}(x, y) + e_z.$$

Differentiating the above equation with respect to time we get

$$\frac{dH_g}{dt} = \frac{\partial H_g}{\partial x}\dot{x} + \frac{\partial H_g}{\partial y}\dot{y} + \frac{\partial H_g}{\partial z}\dot{z} + \frac{\partial H_g}{\partial e_x}\dot{e}_x + \frac{\partial H_g}{\partial e_y}\dot{e}_y + \frac{\partial H_g}{\partial e_z}\dot{e}_z.$$

Calculating the derivatives and using Eq. (3) we get,

$$\frac{dH_g}{dt} = -\frac{1}{2}\frac{\partial \bar{u}}{\partial x} - \frac{1}{2}\frac{\partial \bar{u}}{\partial y} + 0 + 0 + 0 + \left(\frac{1}{2}\frac{\partial \bar{u}}{\partial x} + \frac{1}{2}\frac{\partial \bar{u}}{\partial y}\right) = 0.$$

Hence, H_g is a constant of motion. If angular variables θ and ϕ are used for the particle orientation in place of

e_x, e_y and e_z , then the constant of motion transforms to

$$H_g = -\frac{1}{2}\bar{u}(x, y) - \cos\theta \cos\phi.$$

Appendix B: Comparison of exact versus approximate flow field for Poiseuille flow in a square cross-section

The dimensionless flow field $\bar{u}(x, y)$ used in this paper is an approximation to the following exact flow field for Poiseuille flow in a straight duct with a square cross-section [32]:

$$\bar{u}_e(x, y) = \bar{U}_e(1 - y^2) + \frac{32\bar{U}_e}{\pi^3} \sum_{n=0}^{\infty} \frac{(-1)^{n+1} \cosh\left((2n+1)\frac{\pi x}{2}\right) \cos\left((2n+1)\frac{\pi y}{2}\right)}{(2n+1)^3 \cosh\left((2n+1)\frac{\pi}{2}\right)}. \quad (\text{B1})$$

Here $\bar{U}_e = \bar{U} / \max\{\bar{u}_e(x, y)\} = \bar{U} / \bar{u}_e(0, 0)$, to match the maximum flow speed of \bar{U} at the center of the channel. A comparison of the flow field \bar{u} and \bar{u}_e for $\bar{U} = 1$ is shown in Fig. 12. We see that the overall qualitative flow field is captured well by our approximate flow field \bar{u} and the difference between the two flow fields is small; at most 6% when scaled by the maximum flow speed at the center. Further, we note that the regions in the cross-section where the most significant difference is observed in the flow field are near the corners of the square.

Figure 13 shows the different types of active particle trajectories realized for a more accurate flow field $\bar{u}_e(x, y)$ for Poiseuille flow in a straight channel with square cross-section. Comparing with Fig. 4(a), which used a simpler approximation of the flow field $\bar{u}(x, y)$, we find noticeable differences mainly in the yellow regions. This is to be expected since at these locations, the difference between the flow fields \bar{u}_e and \bar{u} is the largest (see Fig. 12(c)).

-
- [1] E. M. Purcell, Life at low Reynolds number, *American Journal of Physics* **45**, 3 (1977).
- [2] J. Deseigne, O. Dauchot, and H. Chaté, Collective motion of vibrated polar disks, *Phys. Rev. Lett.* **105**, 098001 (2010).
- [3] R. Golestanian, T. B. Liverpool, and A. Ajdari, Designing phoretic micro- and nano-swimmers, *New J. Phys.* **9**, 126 (2007).
- [4] Y. Couder, S. Protière, E. Fort, and A. Boudaoud, Dynamical phenomena: Walking and orbiting droplets, *Nature* **437**, 208 (2005).
- [5] R. N. Valani, A. C. Slim, and T. Simula, Superwalking droplets, *Phys. Rev. Lett.* **123**, 024503 (2019).
- [6] B. V. Hokmabad, R. Dey, M. Jalaal, D. Mohanty, M. Almukambetova, K. A. Baldwin, D. Lohse, and C. C. Maass, Emergence of bimodal motility in active droplets, *Phys. Rev. X* **11**, 011043 (2021).
- [7] J. Elgeti, R. G. Winkler, and G. Gompper, Physics of microswimmers—single particle motion and collective behavior: a review, *Rep. Prog. Phys.* **78**, 056601 (2015).
- [8] Marcos, H. C. Fu, T. R. Powers, and R. Stocker, Bacterial rheotaxis, *PNAS* **109**, 4780 (2012).
- [9] J. E. Simons and S. D. Olson, Sperm motility: Models for dynamic behavior in complex environments, in *Cell Movement: Modeling and Applications*, edited by M. Stolarska and N. Tarfulea (Springer International Publishing, Cham, 2018) pp. 169–209.
- [10] J. C. Conrad and R. Poling-Skutvik, Confined flow: Consequences and implications for bacteria and biofilms, *Annu. Rev. Chem. Biomol. Eng.* **9**, 175 (2018).
- [11] Z. Wu, Y. Chen, D. Mukasa, O. S. Pak, and W. Gao, Medical micro/nanorobots in complex media, *Chem. Soc. Rev.* **49**, 8088 (2020).
- [12] K. Ishimoto, Jeffery's orbits and microswimmers in flows: A theoretical review, *JPSJ* **92**, 062001 (2023).
- [13] A.-I. Bunea and R. Taboryski, Recent advances in microswimmers for biomedical applications, *Micromachines* **11** (2020).

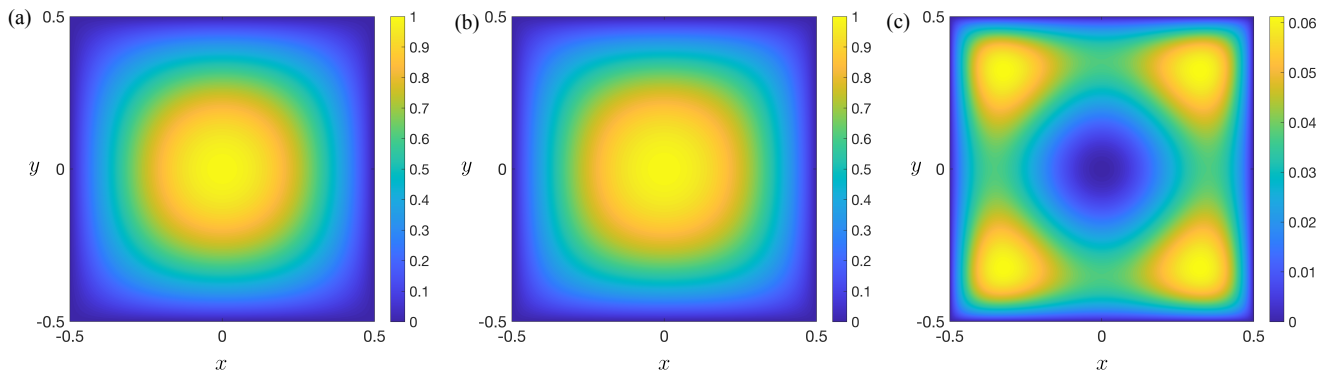


FIG. 12. Comparison of (a) simpler flow field approximation $\bar{u}(x, y)$ as in Eq. (8) used in this paper with (b) a more accurate flow field $\bar{u}_e(x, y)$ as in Eq. (B1) with $n = 100$ terms for Poiseuille flow in a 3D square duct. The difference $\bar{u}_e(x, y) - u(x, y)$ is shown in panel (c).

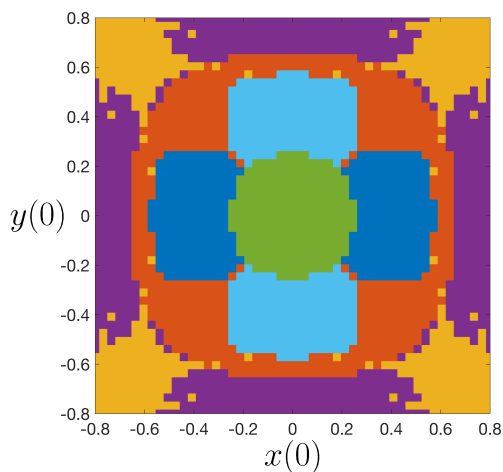


FIG. 13. Classification of active particle trajectories in the initial condition $(x(0), y(0))$ plane using a more accurate flow field in the square cross-section $\bar{u}_e(x, y)$ (as per Eq. (B1) with $n = 100$ terms) compared to the simpler flow field $\bar{u}(x, y)$ used in the paper as in Fig. 4. We note that the grid resolution here is 50×50 compared to the 100×100 resolution in Fig. 4. Other parameters were fixed to $\theta(0) = 0$, $\phi(0) = 0$ and $\bar{U} = 10$.

- [14] D. Zhang, H. Bi, B. Liu, and L. Qiao, Detection of pathogenic microorganisms by microfluidics based analytical methods, *Anal. Chem.* **90**, 5512 (2018).
- [15] D. Matsunaga, F. Meng, A. Zöttl, R. Golestanian, and J. M. Yeomans, Focusing and sorting of ellipsoidal magnetic particles in microchannels, *Phys. Rev. Lett.* **119**, 198002 (2017).
- [16] A. Zöttl and H. Stark, Nonlinear dynamics of a microswimmer in poiseuille flow, *Phys. Rev. Lett.* **108**, 218104 (2012).
- [17] R. Chacón, Chaotic dynamics of a microswimmer in poiseuille flow, *Phys. Rev. E* **88**, 052905 (2013).
- [18] A. J. T. M. Mathijssen, T. N. Shendruk, J. M. Yeomans, and A. Doostmohammadi, Upstream swimming in microbiological flows, *Phys. Rev. Lett.* **116**, 028104 (2016).
- [19] M. Tarama, Swinging motion of active deformable particles in poiseuille flow, *Phys. Rev. E* **96**, 022602 (2017).
- [20] A. Choudhary, S. Paul, F. Rühle, and H. Stark, How inertial lift affects the dynamics of a microswimmer in Poiseuille flow, *Commun. Phys.* **5**, 14 (2022).
- [21] A. Choudhary and H. Stark, On the cross-streamline lift of microswimmers in viscoelastic flows, *Soft Matter* **18**, 48 (2022).
- [22] A. Zöttl and H. Stark, Periodic and quasiperiodic motion of an elongated microswimmer in poiseuille flow, *Eur. Phys. J. E* **36**, 4 (2013).
- [23] A. Zöttl, Hydrodynamics of microswimmers in confinement and in Poiseuille flow (2014).
- [24] Y. Xia and G. M. Whitesides, Soft lithography, *Annu. Rev. Mater. Sci.* **28**, 153 (1998).
- [25] S. H. Strogatz, *Nonlinear Dynamics and Chaos: With Applications to Physics, Biology, Chemistry, and Engineering*, 2nd ed. (CRC Press, 2015).
- [26] B. N. Radhakrishnan, A. Purushothaman, R. Dey, and S. P. Thampi, Confinement induced three-dimensional trajectories of microswimmers in rectangular channels (2023), arxiv:2311.05757.
- [27] G. M. Zaslavsky, *Hamiltonian chaos and fractional dynamics* (Oxford University Press, London, England, 2005).
- [28] V. Afraimovich and G. M. Zaslavsky, Sticky orbits of chaotic Hamiltonian dynamics, in *Chaos, Kinetics and Nonlinear Dynamics in Fluids and Plasmas*, edited by S. Benkadda and G. M. Zaslavsky (Springer Berlin Heidelberg, Berlin, Heidelberg, 1998) pp. 59–82.
- [29] B. Harding, Y. M. Stokes, and A. L. Bertozzi, Effect of inertial lift on a spherical particle suspended in flow through a curved duct, *Journal of Fluid Mechanics* **875**, 1–43 (2019).
- [30] R. N. Valani, B. Harding, and Y. M. Stokes, Bifurcations and dynamics in inertial focusing of particles in curved rectangular ducts, *SIADS* **21**, 2371 (2022).
- [31] R. N. Valani, B. Harding, and Y. M. Stokes, Bifurcations in inertial focusing of a particle suspended in flow through curved rectangular ducts (2021), arXiv:2112.04658.
- [32] M. O. Deville, *An Introduction to the Mechanics of Incompressible Fluids* (Springer International Publishing, 2022).